PHYSICAL REVIEW B

CONDENSED MATTER

THIRD SERIES, VOLUME 39, NUMBER 15 15 MAY 1989-II

Trajectory analysis of low-energy and hyperthermal ions scattered from Cu(110)

R. L. McEachern, D. M. Goodstein, and B. H. Cooper

Laboratory of Atomic and Solid State Physics, Clark Hall, Cornell University, Ithaca, New York 14853

(Received 11 August 1988)

We have investigated the trajectories of Na^+ ions scattered from the Cu(110) surface in the $\langle 1\bar{1}0 \rangle$ and $\langle 001 \rangle$ azimuths for a range of incident energies from 56 eV to 4 keV. Our goal is to explain the trends observed in the energy spectra and determine what types of trajectories contribute to these spectra. Using the computer program SAFARI, we have performed simulations with trajectory analyses for 100-, 200-, and 400-eV scattering. We show results from the 100-eV simulations in both azimuths and compare them with the experimental data. The simulated energy spectra are in excellent agreement with the data. Ion trajectories and impact parameter plots from the simulations are used to determine the relative importance of different types of ion–surface-atom collisions. The simulations have shown that the striking differences observed in comparing the $\langle 1\bar{1}0 \rangle$ and $\langle 001 \rangle$ spectra are mostly due to ions which scatter from second-layer atoms. This system exhibits strong focusing onto the second-layer atoms by the first-layer rows, and the focusing is very sensitive to the spacing between the rows. At the lower beam energies, scattering from the second layer dominates the measured spectra.

I. INTRODUCTION

The interactions of energetic ion beams with surfaces have long been a topic of both theoretical and experimental interest, and more recently of considerable technological importance. Relatively few studies have been done of the scattering kinematics of hyperthermal energy (a few hundred eV and below) ions,[1,2] in part because of the experimental difficulties associated with the production of hyperthermal energy beams. Space-charge repulsion within the beam severely limits the distance over which a well-collimated beam of several nanoamps can be transported. There are also theoretical difficulties associated with interpreting the energy spectra of the scattered ions. However, studies in this energy range provide valuable insights into the fundamentals of hyperthermal energy ion-surface interactions. Such insights are important for understanding processes that occur in reactive scattering and the mechanisms of energy dissipation during ion-beam modification of surfaces.

Analysis of the trajectories of scattered and embedded ions is crucial for a detailed understanding of ion-surface interactions. In this paper we discuss trajectories of scattered keV and hyperthermal energy ions. These trajectories often result from complex many-body interactions that are difficult to model analytically, making it necessary to rely on computer simulations. Simulations for low-energy ion scattering (LEIS), in the few hundred eV to several keV energy range, have been successful enough that LEIS has become a widely used technique for investigating properties of surfaces and atom-surface interactions. Shadowing and blocking analyses of ions scattered from the near-surface region are used to probe local surface structure and composition.[3–9] These studies indicate that keV trajectories can be described as binary collisions of the incident ion with individual surface atoms, and that multiple-scattering trajectories can be treated as sequential binary collisions. As the beam energy is lowered, the penetration depth of the scattered ions becomes restricted primarily to the top one or two layers of the crystal. Therefore, if the trajectories can be understood in detail, hyperthermal ion scattering can be used to probe surface composition and short-range order for crystals where it is desirable to isolate the behavior of the top layers. However, as the beam energy is lowered, the longer-range ion–surface-atom interactions become more important to the scattering and the binary-collision approximation may no longer be valid. If this is the case, the question then arises as to whether the ion-surface interaction potential can be described as a sum of pair potentials between the incident ion and individual surface atoms, or whether many-atom effects must be included.

In this paper we present experimental spectra of Na^+ ions scattered from the Cu(110) surface for energies ranging from 56 to 4 keV. The two principal azimuths of Cu(110), the $\langle 001 \rangle$ and $\langle 1\bar{1}0 \rangle$, differ from one another in

 ©1989 The American Physical Society

the atomic spacing along the rows and separation between the rows of surface atoms, enabling us to compare scattering kinematics for different local atomic arrangements as the incident-beam energy is varied by a factor of 70. As the data show (Figs. 3 and 4), the scattering depends strongly on the crystal azimuth. We have obtained excellent fits to the measured hyperthermal energy spectra with our scattering simulation. The results of trajectory analysis explain the energy-dependent trends in the scattering along the $\langle 001 \rangle$ and $\langle 1\bar{1}0 \rangle$ azimuths. We also show selected examples of K^+ and Ar^+ scattering from Cu(110) to support some of our conclusions from the trajectory analysis.

The remainder of this paper is devoted to discussions of the apparatus, experimental technique, data, and simulations used to interpret these data. In Secs. II and III we give a brief description of the experimental apparatus and our sample cleaning and handling procedures. Section IV is a general discussion where we review some features of ion scattering that are important for understanding our data. In Sec. V we present the scattering data and results of the hyperthermal energy simulations, including trajectory analysis and impact-parameter plots of the scattered ions. We end with a summary of our major conclusions.

II. EXPERIMENTAL APPARATUS

The experimental apparatus is described in detail elsewhere.[10] Here we give only the features that are essential for understanding the work presented in this paper.

The experimental system consists of a gas or alkali-metal-ion source and differentially pumped beamline attached to a two-tiered ultrahigh-vacuum (UHV) scattering chamber which has a base pressure in the mid-10^{-11}-Torr range and typical operating pressures of (1–2) $\times 10^{-10}$ Torr. The upper tier is used for sample preparation and characterization, and includes a sputter gun, an Auger spectrometer, low-energy electron-diffraction (LEED) optics, a Kelvin probe, gas and alkali-metal deposition capabilities, and a residual-gas analyzer.

The ion beam enters the lower tier of the chamber, which houses the 180° spherical electrostatic analyzer used to detect the scattered ions. A pair of apertures at the input of the analyzer limits the angular acceptance to $\pm 1°$ and gives an energy resolution $\Delta E/E$ of 1%. The detector rotates in a horizontal plane about an axis on chamber center, where the sample is located. The sample manipulator provides three independent rotations: 360° about the vertical axis of the manipulator, $\pm 130°$ azimuthal rotation, and 0°–90° tilt. The tilt and azimuth adjustments are accurate to better than 0.5°, while the other manipulator rotation and the detector rotation are accurate to 0.1°. These combined detector and sample rotations and tilt allow access to all scattering geometries except those excluded by the finite size of the detector and lenses.

The beam energy can be varied from approximately 10 eV to 10 keV with an energy spread of less than 0.5 eV. Above a few hundred eV the beam diameter at the sample position is approximately 1 mm and the angular divergence of the beam is $< 1°$. Depending on the energy of the beam, currents from a few nanoamps to hundreds of nanoamps can be delivered to the sample. Special optics were designed to produce well-characterized beams at energies below 400 eV where space-charge spreading is a particular concern. A typical 100-eV beam has a diameter of ≈ 3 mm, an angular divergence of $\pm 1°$–$2°$, and a current of 2–3 nA.[11]

To obtain accurate energy spectra, it is crucial that the rotation axes of the manipulator and detector coincide. In addition, the central axis of the beamline optics must intersect these rotation axes. The technique used to achieve this is described in Ref. 10. Linear alignment between the different elements inside the chamber was achieved to 0.25-mm accuracy, and angular alignment to better than 0.5° accuracy, both of which are smaller than the width and angular divergence of the ion beam. The alignment was verified experimentally by first measuring a spectrum along one of the principal azimuths of the sample with the detector at a chosen scattering angle. Both the sample and detector were then rotated to their mirror positions about the plane intersecting the beam axis and the vertical axis through the chamber center. A second spectrum was measured in this mirror position. Experimentally we found that the energies of the peaks in these two spectra agreed to within a few tenths of a percent.

LEED was used to position the crystal to within $\pm 2°$ of the orientation required for scattering along the $\langle 001 \rangle$ or $\langle 1\bar{1}0 \rangle$ azimuth. A more accurate orientation was determined by measuring energy spectra over a range of azimuthal angles spanning the approximate $\langle 1\bar{1}0 \rangle$ orientation. The symmetry of the spectra on either side of this orientation allowed us to position the sample azimuth to within $\pm 0.5°$. Fiducial marks are attached to the sample so the angular position can be recorded and set easily from outside the vacuum.

An energy spectrum is obtained by ramping the voltages on the hemispheres of the detector. The energy-analyzed particles are counted by an electron multiplier operated in the pulse-counting mode. To ensure that readings from different bins of the energy spectrum correspond to the same incident-ion dose, the current on target is monitored continuously during an energy scan. Between spectra a Faraday cup, mounted below the sample on the sample manipulator, is placed at the sample position to obtain a reliable measurement of the incident current. In practice, the beam current is very stable, usually varying less than a few percent over several spectra. The Faraday cup has a 1-mm aperture whose position relative to the sample center is known precisely, so the Faraday cup is also used to position the beam accurately on the center of the sample.

III. SAMPLE HANDLING

The single-crystal copper sample used in these experiments was aligned using x-ray diffraction, then cut and mechanically polished to make a 2-mm-thick–by–8.7-mm-diam disc within 1° of the (110) surface orientation.[12] This sample was then mounted on a button heater, which contains a filament for resistive heating.

The sample was initially cleaned by cycles of sputtering

with 500-eV Ar^+ ions and annealing at 650 °C, which brought primarily sulfur and antimony to the surface. This was repeated until an Auger measurement detected no contamination following a 30-min anneal at 550 °C. Extended anneals at 650 °C still produced traces of sulfur, but no evidence of antimony.

After the initial cleaning period, the standard cleaning procedure was to sputter the sample uniformly with 1.5 μA of 500-eV Ar^+ for 30 sec followed by a 30-min anneal at 550 °C. LEED was used to verify that this anneal was sufficient to restore surface order following the sputter cycle. The ion-scattering experiments were performed at room temperature.

During data collection using alkali-metal beams the sample was monitored both for surface damage and for contamination from the incident beam. The total beam dose per spectrum at 100 eV was 1.9×10^{13} Na^+-ions/cm^2. No degredation in the spectra was seen from sputter damage by the Na beam. The amount of Na deposited on the sample surface was monitored with Auger spectroscopy. After a sufficiently long exposure to the beam, the Na deposited in the sample resulted in increased neutralization of the scattered beam due to an increase in the resonant charge-transfer probability.[13] Investigation of this effect showed that the neutralization was trajectory independent, so the relative heights of peaks in the energy spectra were unaffected. These results are described in detail elsewhere.[14]

IV. SIMULATION

To interpret our experimental results for beam energies of several hundred eV or lower, we use the computer code SAFARI.[15] This program solves Hamilton's equations of motion for ions interacting with surfaces; a simulation of the scattered-ion spectrum is formed by combining ion trajectories with impact parameters distributed over the unit cell. We use an ion-surface potential that is composed of an image potential and a sum of ion–surface-atom pair potentials. At each point in the calculation of an ion trajectory, typically five to eight surface atoms are included in this sum. A major question in simulating hyperthermal energy scattering concerns the ion-surface interaction potential. This has been the topic of recent theoretical and experimental interest.[1,2,16,17] We have achieved very good agreement between measured and simulated energy spectra for the 100- [see Figs. 5(a) and 6(a)], 200-, and 400-eV Na^+-ion beams using a sum of Na^+-Cu pair potentials, where the sum runs over six surface atoms at any one time. An image potential is added to this which depends only on distance from the surface. The pair potential was a sum of two exponential terms (with four parameters). The four parameters were chosen to fit a Na^+-Cu pair calculation using the Hartree-Fock approximation.[18] The two-exponential potential agrees with the Hartree-Fock potential to within a few percent at all the relevant Na^+-Cu separations, approximately 0.6–2 Å. The only adjustable parameter in our potential is the well depth of the image potential, i.e., the limiting value of the image potential as the ion approaches the surface. In the 100-eV simulation, its main effect is a shift of the spectrum to lower energies for larger well depths (changing the well depth from 0 to 4 eV causes a shift on the order of 3 eV). The relative peak heights remain nearly unchanged. For the 200- and 400-eV simulations, varying the well depth has almost no effect on the spectra. The well depth was chosen as a best fit for the 100-eV Na^+ spectra; the same value was used for the 200- and 400-eV simulations. For a detailed discussion of this potential, we refer the reader elsewhere.[19]

In our simulations we assumed no angular divergence of the beam. The angular acceptance of the simulated detector was 2°. Thermal vibrations were included by assigning appropriately distributed initial velocities and displacements (with a rms vibration amplitude of 0.08 Å) to the surface atoms. The two variables are uncorrelated. A 7.5% inward relaxation of the first atomic layer was used.[20] Increasing the second- to third-layer spacing by up to 2.5% had almost no effect on the simulation, so the bulk spacing was generally used.

Results from SAFARI calculations are presented in Sec. VI. We use three types of SAFARI output: individual trajectory calculations, energy spectra, and impact-parameter plots. The first two are self-explanatory; below we describe how SAFARI generates impact-parameter plots. In calculating representative trajectories for a given ion-surface combination and scattering geometry, SAFARI uses an adaptive-grid technique for choosing incident-ion impact parameters. This technique makes use of two aspects of spectrum computation. The first is that ion trajectories change more rapidly with impact parameter in certain regions of the unit cell than in others. The second is that most of the unit cell does not contribute to a given measured spectrum. The adaptive-grid technique distributes impact parameters throughout the surface unit cell. The grid on which these impact parameters lie is nonuniform, with a different grid size in different parts of the unit cell. The grid spacing is smallest where the impact parameters produce scattering within a specified range of final angles (the "detector"). Trajectories which scatter into the detector are then weighted according to the fraction of the unit cell represented by the grid spacing from which they originated. From these grids impact-parameter plots can be generated that represent the distribution within the surface unit cell of impact parameters that contributed to the spectrum (Figs. 9–11). SAFARI also has the option of choosing impact parameters with a Monte Carlo selector. Spectra generated with the Monte Carlo and adaptive-grid–size techniques show very good agreement with one another.

V. GENERAL DISCUSSION

The SAFARI simulations include simultaneous ion-surface interactions, which are necessary for quantitative modeling of hyperthermal energy scattering. However, a qualitative understanding of the energy spectra is possible using the sequential binary-collision approximation. In other words, by viewing each trajectory as a series of pure binary collisions between the ion and one or more surface atoms, the total energy loss of the scattered ion can be *approximately* calculated by simply adding up the kinematic losses associated with each collision. This ap-

proximation cannot be applied effectively to all hyperthermal trajectories; in some cases, the incident ion collides nearly simultaneously with multiple surface atoms. This approximation also ignores the image potential which, according to our simulations, can measurably affect the final energy of the scattered ion for incident energies below about 200 eV. Keeping in mind that the assumption of sequential binary collisions is an approximation, we will use it to simplify the discussion of our experimental results.

In this context it is useful to review some basic features of binary collisions. Figure 1 shows a plot of the kinematic factor (E_f/E_0) versus total scattering angle ϕ for a sodium ion of mass 23 and initial energy E_0 colliding with a stationary copper atom of mass 63.5. The final energy of the scattered sodium is E_f. The kinematic factor is determined by momentum and energy conservation; it is independent of the form of the interaction potential. The dashed line shows $(\partial/\partial\phi)(E_f/E_0)$, and illustrates the important point that for small scattering angles ($\lesssim 10°$) the kinematic factor is relatively insensitive to small changes in ϕ, while for larger scattering angles ($20° < \phi < 120°$) it is a strong function of ϕ. For example, a sodium ion scattering through a 5° angle from a copper atom experiences an energy loss of only 0.27%, whereas changing the scattering angle from 89° to 90° for the same pair changes the energy loss from 46.8% to 47.5%, a difference of 0.7%. A practical consequence of this functional behavior is that for trajectories consisting of a combination of small- and large-angle collisions E_f is determined almost entirely by the large-angle collision(s).

When ions scatter from a single-crystal surface, many kinds of trajectories are possible. However, it is frequently observed that for a given scattering geometry and incident energy most of the scattered intensity is due to only a few types of trajectories. There are two types, in particular, which are most important for the energy range and scattering geometries discussed in this paper: single collisions and double collisions. The lowest-energy peak observed in a spectrum is usually due to single-scattering trajectories. This also is a consequence of the functional form of the kinematic factor; that is, a particle undergoing multiple in-plane forward collisions will experience a smaller energy loss then one undergoing a single collision through the same total scattering angle. Quasisingle (QS) trajectories occur when the incident ion has small angle in-plane collisions with atoms adjacent to the principal target atom before and after the main impact, decreasing the total energy loss. At lower incident energies the long-range part of the potential becomes more important and the effect of these small-angle collisions becomes more pronounced.

The highest-energy scattered ions are usually those associated with double scattering, i.e., trajectories involving two large-angle collisions. The minimum energy loss $(E_f/E_0)_{\max}$ for this type of trajectory occurs with two equal-angle collisions. For specular scattering, especially at higher incident energies, the measured high-energy peak actually falls close to this value. There is also a wide variety of possible zig-zag trajectories. While most of these have lower final energies than a trajectory with two equal-angle forward collisions, it is possible to have zig-zags involving more than two collisions which appear at higher final energies. However, we have not found a significant contribution from such high-energy zig-zag trajectories.

VI. RESULTS

Figure 2 shows the atom positions on the Cu(110) surface, and defines the angles used to specify our scattering geometry. Figures 3 and 4 show sets of energy spectra for Na^+ ions scattered along $\langle 1\bar{1}0 \rangle$ (Fig. 3) and $\langle 001 \rangle$ (Fig. 4) azimuths of Cu(110) for incident beam energies ranging from 56 eV to 4 keV. For all these spectra the angle of incidence θ for the incoming beam is 45° and the total scattering angle ϕ is 90°. Normalized intensity with an arbitrary zero offset is plotted along the vertical axis.

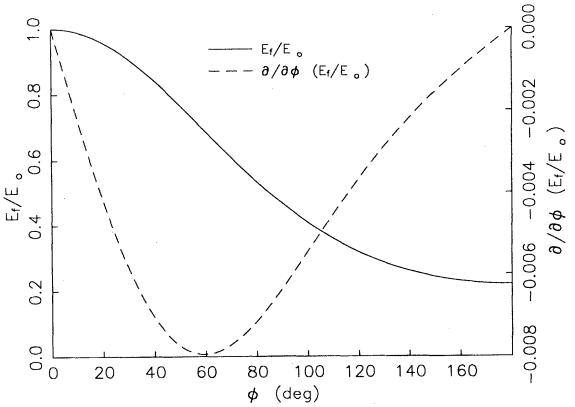

FIG. 1. Kinematic factor and its derivative for a mass-23 particle scattered from a mass-63.5 particle through an angle ϕ.

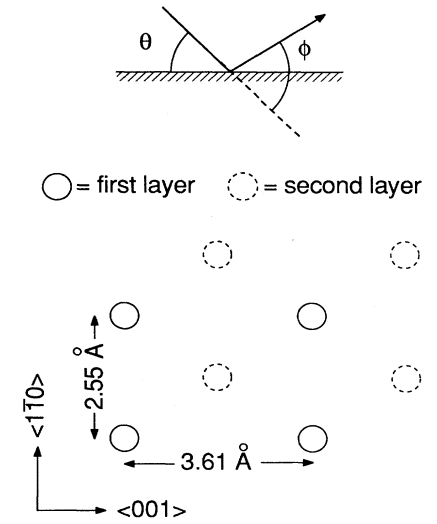

FIG. 2. Schematic representation of the Cu(110) surface showing the two principal azimuths. The angles used to define the scattering geometry are shown above.

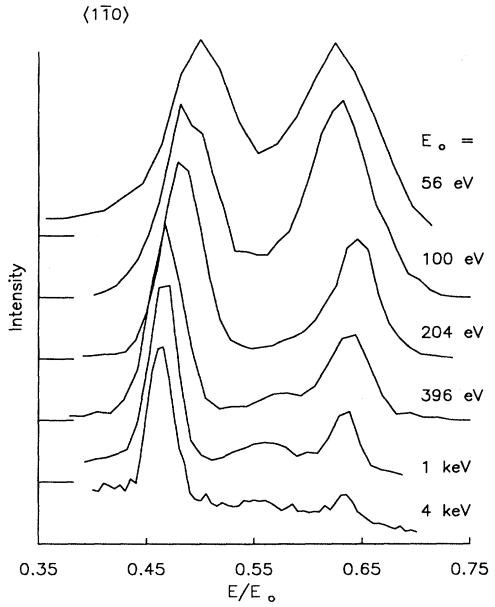

FIG. 3. Intensity vs reduced energy for Na^+ scattered from Cu(110) in the $\langle 1\bar{1}0 \rangle$ azimuth for $\theta=45°$, $\phi=90°$. Incident-beam energy ranges from 56 eV to 4 keV. The spectra are normalized and offset vertically, the tic marks on the vertical axis indicating the zero offset of each successive curve.

Reduced energy E/E_0 is plotted along the horizontal axis, where E is the energy of the scattered ions and E_0 is the incident-beam energy.

Except for differences in relative peak heights, the scattering spectra from the $\langle 1\bar{1}0 \rangle$ azimuth for incident energies ranging from 1 keV to 56 eV look similar to one another. However, in spite of the similar overall shapes of the spectra, computer simulations show that the relative importance of the different types of trajectories which contribute to the peaks changes considerably over this range. In contrast to the $\langle 1\bar{1}0 \rangle$ azimuth, the $\langle 001 \rangle$ spectra look quite different from one another as the incident-beam energy is decreased. This difference is due primarily to focused scattering from the second-layer atoms. In the $\langle 001 \rangle$ direction, between 200 eV and 1 keV, E/E_0 for ions which undergo single scattering from second-layer atoms changes rapidly as a function of incident energy. Below 200 eV the second-layer double scattering also changes rapidly with incident energy. Since both the single and double focused trajectories contribute substantial weight to the total scattered intensity, the measured $\langle 001 \rangle$ spectra show a strong variation with incident energy.

In order to understand the trends in the data in more detail, we have done extensive trajectory analysis using SAFARI simulations at 100, 200, and 400 eV. In this paper we show results from this analysis for the 100-eV simulations; the results from the 200- and 400-eV simulations are qualitatively similar to those at 100 eV. Although the simulated energy spectra shown in Figs. 5 and 6 were calculated including thermal vibrations of the sur-

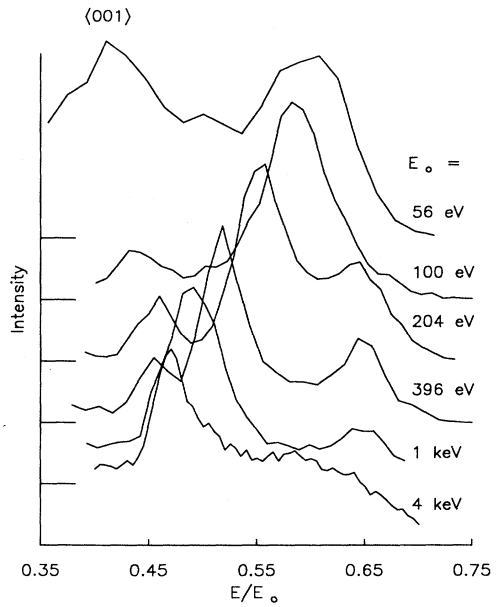

FIG. 4. Same as Fig. 3, expect the beam is incident along the $\langle 001 \rangle$ azimuth.

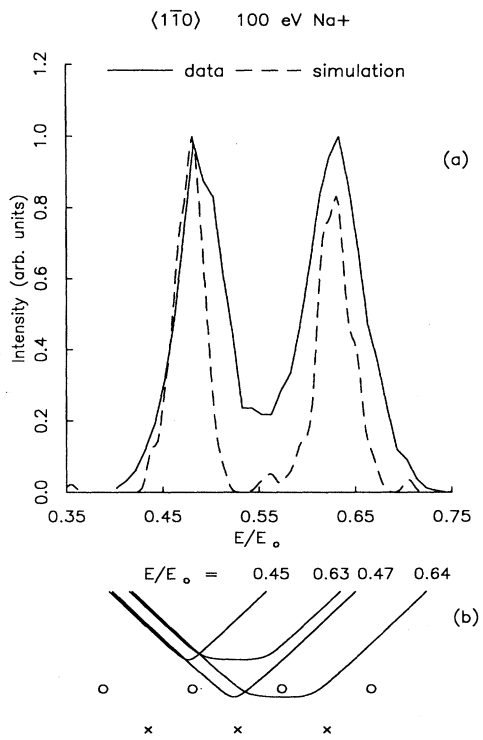

FIG. 5. (a) Comparison between data and simulation for the 100-eV Na^+ spectrum shown in Fig. 3 ($\langle 1\bar{1}0 \rangle$ azimuth). (b) Side views of representative trajectories from the simulated spectrum. The reduced energy of each trajectory is shown. Top-layer atoms are denoted by circles, second-layer atoms by crosses.

face atoms, the trajectory analyses were taken from simulations without thermal vibrations. This simplifies the analysis and does not alter our conclusions since thermal vibrations have not been found to introduce any significant new types of trajectories. The principal effects of thermal vibrations are peak broadening and some changes in relative peak intensities.

Figures 5(a) and 6(a) show comparisons between SAFARI simulations and experimental data for 100-eV Na^+ scattering in the $\langle 1\bar{1}0 \rangle$ [Fig. 5(a)] and $\langle 001 \rangle$ [Fig. 6(a)] azimuths. Figures 5(b) and 6(b) show side views of the major types of trajectories which contribute to the spectra in Figs. 5(a) and 6(a); trajectories that contribute little weight, such as the top-layer doubles, are also shown for the purpose of discussion and because they can be more important at higher energies. The technique we use for assigning weights to different trajectories will be discussed later in this section.

At the lowest energies ($E/E_0=0.45$ and 0.44 from Figs. 5 and 6, respectively) are the trajectories resulting from single scattering off of first-layer atoms. At $E/E_0=0.47$ and 0.58 are the "focused single" trajectories, which arise when the first layer rows of atoms focus incident ions onto a second-layer atom.[21,22] Depending on the crystal geometry, this focusing can occur over a broad range of impact parameters, thereby enhancing the intensity of the scattering from the second-layer atom. At $E/E_0=0.64$ and 0.56 are the focused double trajectories, which arise in a manner similar to the focused singles. There are also some contributions from top-layer doubles ($E/E_0=0.63$) and zig-zag trajectories (various energies). We will now discuss these different trajectories in greater detail.

As mentioned earlier, single-scattering trajectories experience the greatest energy loss of any in-plane top-layer trajectory. Note, however, that for the 100-eV trajectories shown in Figs. 5(b) and 6(b) the top-layer QS collision energies are different in the two azimuths, and both are below the kinematic value of $E/E_0=0.468$. The energies of these trajectories are influenced by two competing effects: the image charge and the increasingly "quasi" nature of the collision at low incident energies. The latter effect decreases the energy loss as explained in Sec. V. The image force increases the energy loss in two ways. First, it accelerates the ion, causing it to hit the surface harder and lose more energy. Second, because the ion accelerates towards the surface before the principal collision and decelerates afterwards, the total scattering angle of the principal collision is slightly larger than it would be in the absence of the image charge. This also increases the energy loss. Although the image potential is a function only of the ion-surface distance, the effect of top-layer quasiscattering is more pronounced in the $\langle 1\bar{1}0 \rangle$ azimuth where the atoms are closer together than in the $\langle 001 \rangle$ direction. This results in the QS trajectories appearing at higher energies in the $\langle 1\bar{1}0 \rangle$ azimuth.

Now consider the second-layer focused single-scattering trajectories. These occur when incident ions have impact parameters between the rows of top-layer atoms and experience small-angle collisions with first-layer atoms before and/or after the main impact with a second-layer atom. Because these trajectories need not remain in plane, there are many possible paths that scatter into the detector. This is demonstrated graphically in Fig. 7, which is a top view of some of the focused single (FS) trajectories from the 100-eV $\langle 1\bar{1}0 \rangle$ simulation. Focusing can have a very strong influence on the spectra; in both azimuths, the contribution from focused singles substantially outweighs that of top-layer single scattering. However, the FS trajectories differ considerably from one another in the two azimuths (see below).

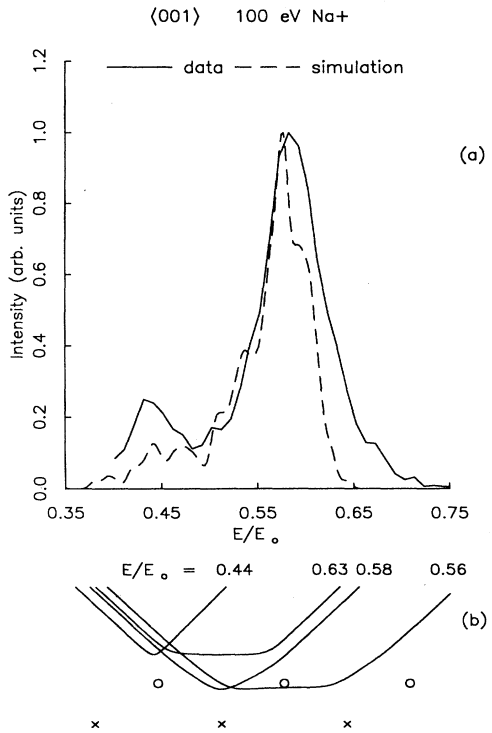

FIG. 6. (a) Data vs simulation for the 100-eV spectrum in Fig. 4 ($\langle 001 \rangle$ azimuth). (b) Same as Fig. 5(b), but for the $\langle 001 \rangle$ azimuth.

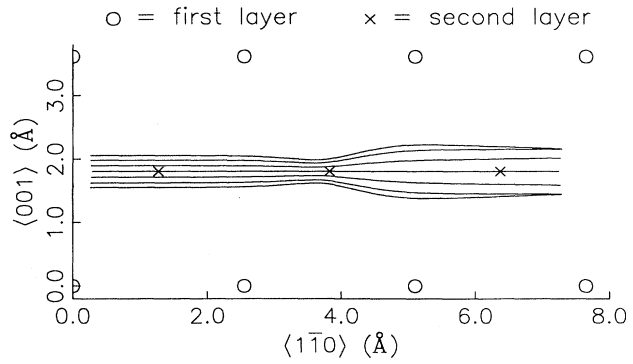

FIG. 7. Top view of focused single trajectories from the 100-eV $\langle 1\bar{1}0 \rangle$ simulation. The principal collision is with the second-layer atom at $\langle 1\bar{1}0 \rangle = 3.83$.

There are two aspects of the FS scattering which should be noted. First, even ions which have a completely in-plane trajectory, i.e., are incident precisely over the second-layer rows, scatter from first-layer atoms. Second, although ions over a considerable range of impact parameters can experience FS trajectories, there is not an excessively large energy spread associated with a group of FS trajectories for a given azimuth. This follows from the fact that for all the FS trajectories in one azimuth the principal collision is almost the same, and this is where most of the energy loss occurs. The small-angle out-of-plane collisions have very little energy loss associated with them (see Fig. 1 and related discussion). In other words, the forces transverse to the scattering plane, which can vary considerably for the different FS trajectories, have little effect on the final energy. The in-plane forces are much more important in determining the final energy.

Since most of the energy loss in a FS trajectory occurs during the second-layer collision, any change in the local atomic positions which affects this second-layer impact will result in an energy shift. The rows in the ⟨001⟩ direction are relatively close together (2.55 Å), so the incoming ion encounters substantial in-plane forces from each of the first-layer atoms on either side of a second-layer row. In the ⟨1$\bar{1}$0⟩ direction the rows are farther apart (3.61 Å), considerably lessening this effect. Figure 8 shows a comparison between the 100-eV focused single trajectories in the two azimuths. The ⟨001⟩ scattering clearly shows a much greater modification of the in-plane trajectory by the first layer rows. As a consequence, the 100-eV FS trajectories in the two azimuths are at different energies ($E/E_0=0.47$ in the ⟨1$\bar{1}$0⟩, $E/E_0=0.58$ in the ⟨001⟩).

The azimuth-dependent behavior of the FS trajectories is largely responsible for the qualitative differences observed in the two sets of spectra shown in Figs. 3 and 4.

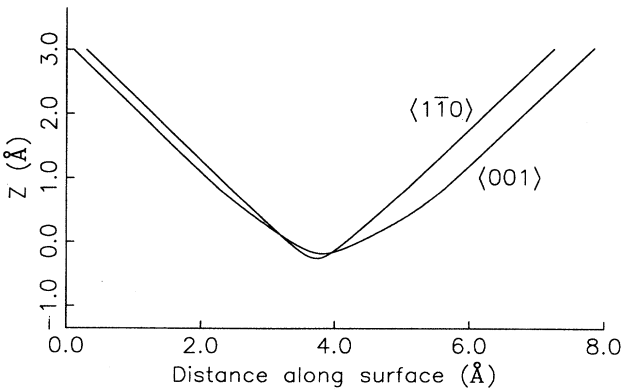

FIG. 8. Side view of the focused single trajectories in the ⟨1$\bar{1}$0⟩ and ⟨001⟩ azimuths. The first atomic layer is at $Z=0$, and, due to the surface relaxation, the second layer is at $Z=-1.18$. The ⟨001⟩ trajectory has been offset 1.59 Å to the left, so the second-layer atom with which the main impact occurs is at the same coordinate as the corresponding second-layer atom in the ⟨1$\bar{1}$0⟩ azimuth.

In the ⟨1$\bar{1}$0⟩ azimuth, the second-layer FS and top-layer QS trajectories are close enough in energy that they cannot be resolved as separate peaks at any of the incident energies shown in Fig. 3, and above 200 eV they both fall very close to the kinematic single-scattering value. However, in the ⟨001⟩ azimuth the 100-eV FS trajectories are close in energy to the focused doubles at $E/E_0=0.56$, well above the QS peak. As the beam energy is increased, the ⟨001⟩ FS collision becomes less "quasi," the final energy moves to lower E/E_0, and the FS peak becomes clearly resolved. At 1 keV the QS and FS peaks have merged, and by 4 keV the two are the indistinguishable.

For incident beam energies of 200 eV and above, the highest-energy trajectories in both azimuths are those associated with double scattering. The peaks related to these trajectories fall near $E/E_0=0.649$, the kinematic value for two 45° collisions. Since most zig-zags fall at or below this value, the presence of zig-zags can lower the peak position below the kinematic value. Below 200 eV the double scattering in both azimuths is dominated by second-layer focused double trajectories. Thus, although the top-layer doubles from the 100-eV spectra [Figs. 5(a) and 6(a)] are very similar ($E/E_0=0.63$ in both azimuths), their contribution to the total scattering is minimal. The focused doubles are quite different in the two azimuths: $E/E_0=0.56$ in the ⟨001⟩, $E/E_0=0.64$ in the ⟨1$\bar{1}$0⟩. Careful examination of the ⟨001⟩ focused double trajectory [see Fig. 6(b)] reveals that between the two principal collisions with adjacent second-layer atoms the incident ion scatters off the first-layer atoms from below. While there is little energy loss in this collision, it slightly increases the scattering angle of each of the main impacts, which has a relatively large effect on the final energy. Below 200 eV the azimuth-dependent behavior of the focused second-layer trajectories, both singles and doubles, is largely responsible for the qualitative differences between the measured spectra in the two azimuths.

As discussed in Sec. IV, SAFARI can be used to generate plots showing which impact parameters result in trajectories that scatter into the simulated detector. Figures 9 and 10 show these plots for 100-eV Na^+-ion scattering along the ⟨1$\bar{1}$0⟩ and ⟨001⟩ azimuths, respectively. The same simulations were used for both the preceding trajectory analysis and these impact-parameter plots. The dark areas indicate the location of impact parameters which scattered into the detector. Although the symmetry of the surface allows the simulation to use only half the area of the unit cell, an entire surface unit cell is shown in Figs. 9 and 10. The axes are labeled in angstroms, with a top-layer atom at ⟨1$\bar{1}$0⟩=0.0, ⟨001⟩=0.0. In Fig. 9 the first-layer rows of the crystal coincide with the left and right edges of the figure and the beam is incident from the bottom. In Fig. 10 the first-layer rows lie along the top and bottom edges and the beam is incident from the left. In both figures the position of the second-layer row is indicated with a dashed line.

Generally, most of the ions which have impact parameters within a localized region on the impact-parameter plot will have similar trajectories and final energies. It is

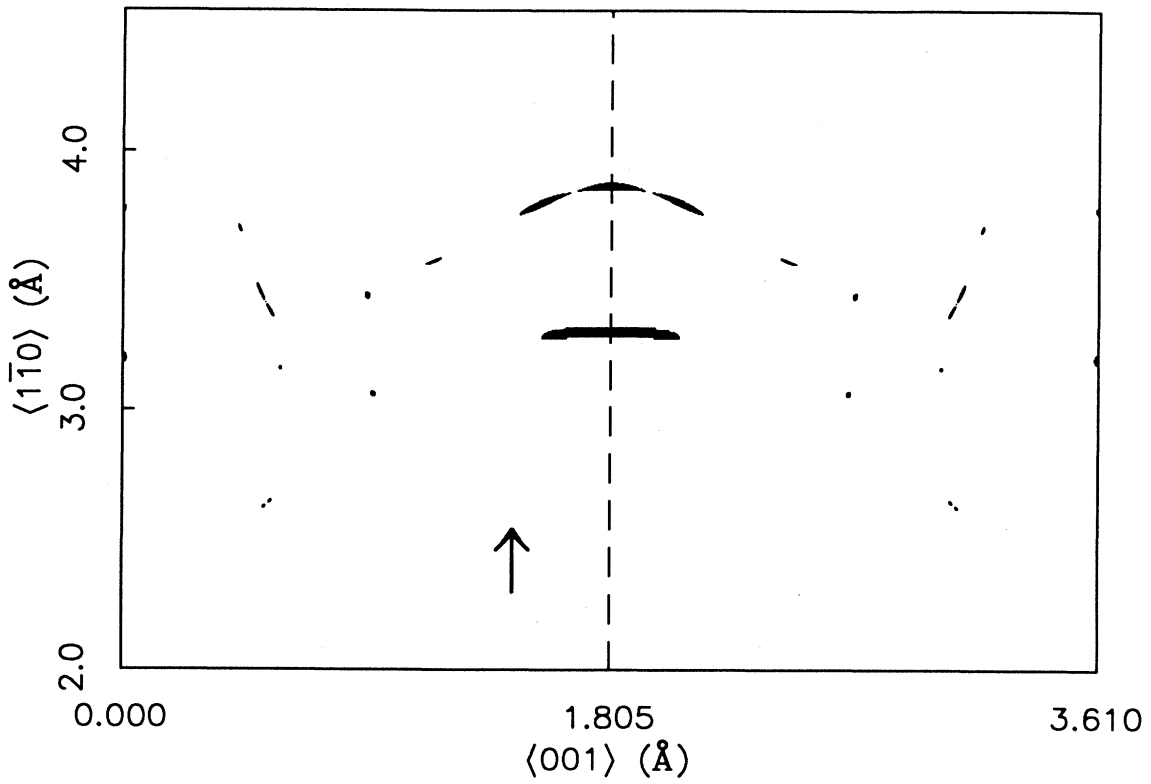

FIG. 9. Impact-parameter plot of a 100-eV Na^+ simulation in the $\langle 1\bar{1}0\rangle$ azimuth for $\theta=45°$, $\phi=90°$ (see text for details). The position of the second-layer atomic row is indicated by the dashed line. The top-layer rows lie along the left and right edges of the plot at $\langle 001\rangle=0.0$ and 3.61. The arrow indicates the direction of the incident beam. This simulation does not include thermal vibrations, and the left half of the plot is simply a reflection of the right half (see text).

therefore often possible to associate peaks in the energy spectra with specific regions in the impact-parameter plot. In Fig. 9 the plot is dominated by two regions centered over the second-layer row. The one at $\langle 1\bar{1}0\rangle=3.3$ represents FS trajectories, while the region at $\langle 1\bar{1}0\rangle=3.85$ corresponds to focused double trajectories.[23] The lobes on either side of the central region are also focused doubles. The top-layer singles and doubles are centered over the first-layer rows at $\langle 1\bar{1}0\rangle=3.2$ and 3.8, respectively. The much larger regions centered over the second-layer atomic rows demonstrate the dominance of the second-layer scattering in the measured spectra. By contrast, in Fig. 10 the FS contribution at $\langle 1\bar{1}0\rangle=1.275$, $\langle 001\rangle=4.65$ does not outweigh that from the top-layer singles ($\langle 001\rangle=4.25$) by as much. The focused doubles ($\langle 001\rangle=5.2$) make the largest contribution in this azimuth. The trajectories at the far ends of the region, $\langle 1\bar{1}0\rangle\approx 0.9$ and 1.65, are actually zig-zags that appear at lower energies, but most of the weight in this region belongs to the focused doubles.

It was stated at the beginning of this section that despite the similarity of the $\langle 1\bar{1}0\rangle$ energy spectra, the relative importance of the different types of trajectories changed substantially at different incident-beam energies. This behavior is reflected in the impact-parameter plots. Figure 11 shows the impact parameters from a simulation of 400-eV Na^+ ions scattered in the $\langle 1\bar{1}0\rangle$ azimuth with $\theta=45°$, $\phi=90°$. Compared to Fig. 9, the contribution of the focused second-layer trajectories is greatly reduced.

So far, the discussion has centered exclusively on Na^+ scattering. However, it is informative to compare spectra for Na^+ and other alkali-metal species to those from noble-gas species. For a noble-gas ion, there is a relatively high probability of neutralization after the particle scatters from a surface. This is in contrast to alkali-metal-ion scattering where the neutralization probabilities, depending on the species and energy, can be very small. These effects can lead to dramatic trajectory-dependent differences in the scattered-ion spectra. For example, due to the high neutralization probabilities of noble-gas species the multiple-scattering trajectories are often suppressed relative to the single-scattering trajectories.

This is illustrated experimentally in Fig. 12, which shows a comparison between 1-keV Ar^+ and 1-keV K^+ ions scattered in the $\langle 001\rangle$ azimuth for 70° specular scattering ($\theta=35°$ and $\phi=70°$). Since K^+ has a mass of 39.1 amu and Ar^+ has a mass of 39.9 amu, the scattering kinematics and distribution of trajectories will be very similar. Although the scattering geometries are different, 70° versus 90° total scattering angle, note that the K^+ spectrum looks quite similar to that of the 1-keV Na^+ spectrum in the $\langle 001\rangle$ azimuth (see Fig. 4). In particular, the structure of the lower-energy peak is quite simi-

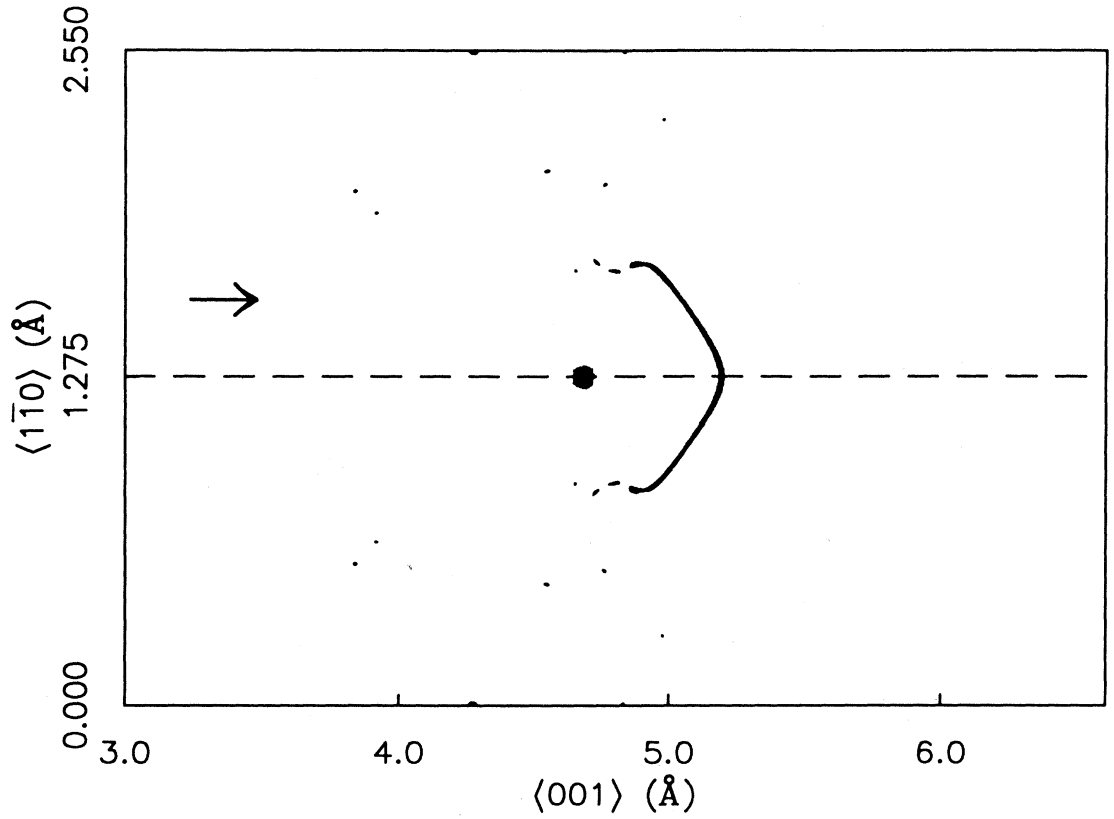

FIG. 10. Same as Fig. 9, except for scattering in the ⟨001⟩ azimuth. The top-layer atomic rows are now along the top and bottom edges at ⟨1$\bar{1}$0⟩=0.0 and 2.55.

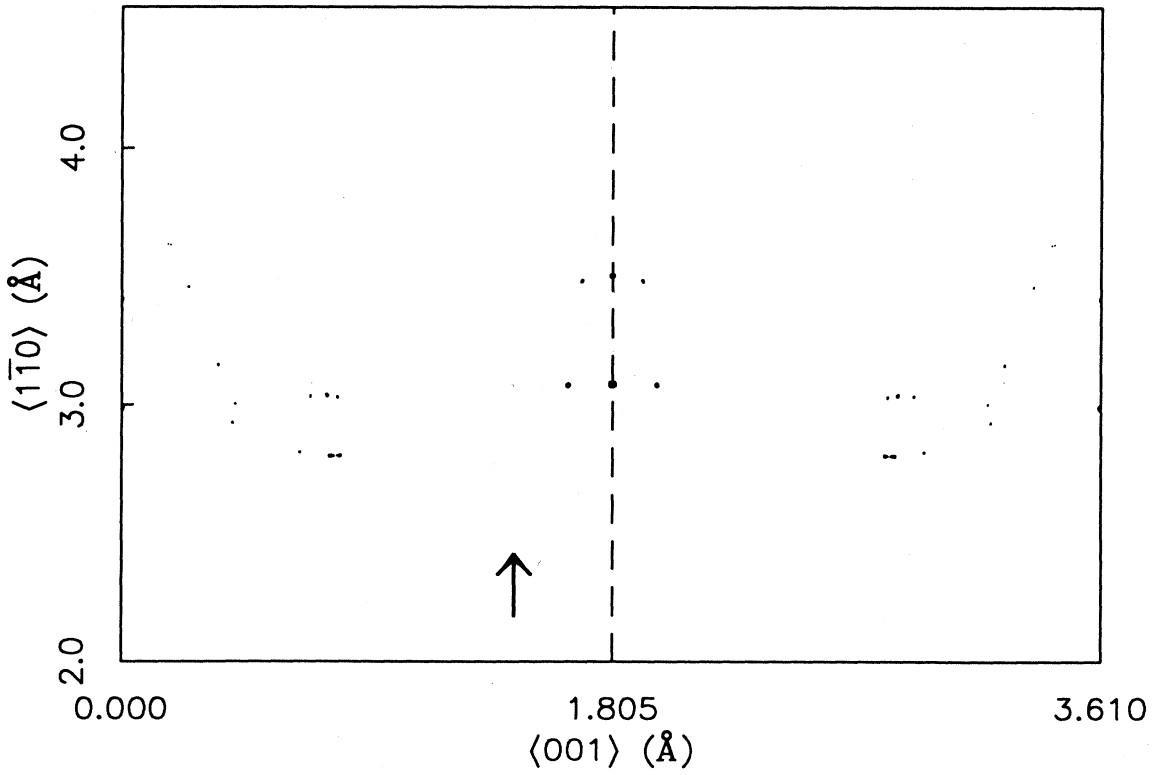

FIG. 11. Same as Fig. 9, except for an incident-beam energy of 400 eV.

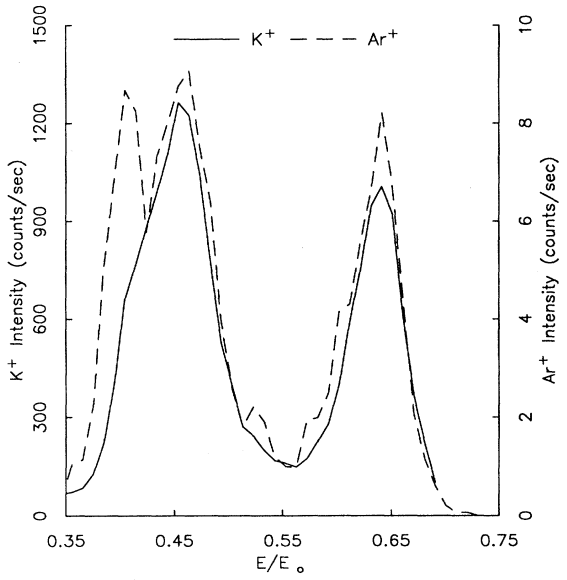

FIG. 12. Comparison between 1-keV K^+ and 1-keV Ar^+ scattering in the $\langle 1\bar{1}0 \rangle$ azimuth for $\theta = 35°$, $\phi = 70°$. The spectra correspond to the same beam current on the target.

lar. It is composed of the contribution from top-layer QS trajectories, at the kinematic energy for single scattering, buried under the much larger peak of the second layer FS trajectories which sit at slightly higher energies. The FS and QS trajectories are close enough in energy that two peaks are not resolved. This is in contrast to the Ar^+ spectrum which shows the QS and FS trajectories as distinct peaks. Since an Ar^+ ion has a high probability of neutralizing during a multiple-scattering trajectory,[4,24] these trajectories are preferentially neutralized compared to the QS trajectories, so the QS peak is relatively much larger. Note, however, that the Ar^+ ions have a sufficiently high survival probability that multiple-scattering features are not totally suppressed. By contrast, Ne^+ and He^+ often show only single-scattering trajectories. Noble-gas scattering is commonly used for surface-composition analyses,[4,25] as well as for structural studies using shadowing and blocking,[5,9] where the additional complication of multiple-scattering features is undesirable.

VII. CONCLUSIONS

We have shown that the kinematics of ion scattering at hyperthermal energies is very sensitive to short-range order, demonstrated by the fact that the energy spectra for hyperthermal Na^+ ions scattered from Cu(110) in the $\langle 001 \rangle$ and $\langle 1\bar{1}0 \rangle$ azimuths are qualitatively different from one another. Using computer simulations of the scattering it is possible to understand in detail the scattered-ion trajectories contributing to these spectra. Over a range of incident-beam energies from 56 eV to 4 keV, the top-layer scattering is similar in the two azimuths. Between 200 eV and 1 keV the second-layer focused single trajectories are largely responsible for the differences between the $\langle 1\bar{1}0 \rangle$ and $\langle 001 \rangle$ spectra. Below 200 eV the second-layer focused double trajectories begin behaving very differently in the two azimuths. Consequently, for beam energies below 200 eV both the focused singles and focused doubles contribute to the contrasting appearance of the energy spectra in the two azimuths. Impact-parameter plots can be used to assign relative weights to the different types of trajectories. These weights are very sensitive to the crystal geometry and incident-beam energy. Impact-parameter plots from the 100-eV simulations show that scattering from second-layer atoms dominates the observed 100-eV spectra in both azimuths. Spectra measured with ion species having different neutralization probabilities demonstrate that it is necessary to understand both single- and multiple-scattering trajectories to interpret the spectra.

ACKNOWLEDGMENTS

The authors would like to acknowledge fruitful discussions with Jim Sethna, Ernie Behringer, and Chris DiRubio. David Adler, Greg Kimmel, and David Peale provided valuable assistance in collecting the data. This work was supported by the National Science Foundation (Grant No. NSF-DMR-84-51979) and by the U.S. Air Force Office of Scientific Research (Grant No. AFOSR-88-0069). The simulations were funded by the National Science Foundation through the Cornell Materials Science Center (Grant No. NSF-DMR-85-16616) and were done on the Cornell Production Supercomputer Facility of the Center for Theory and Simulation in Science and Engineering, which is funded, in part, by the National Science Foundation, New York State, and IBM Corporation.

[1]E. Hulpke and K. Mann, Surf. Sci. **133**, 171 (1983).
[2]A. D. Tenner, K. T. Gillen, T. C. M. Horn, J. Los, and A. W. Kleyn, Surf. Sci. **172**, 90 (1986).
[3]W. Heiland and E. Taglauer, in *Methods of Experimental Physics—Vol. 22. Solid State Physics: Surfaces,* edited by R. L. Park and M. G. Lagally (Academic, Orlando, 1985), Vol. 22, Chap. 6, and references therein.
[4]T. M. Buck, in *Methods of Surface Analysis,* edited by A. W. Czanderna (Elsevier, Amsterdam, 1975), p. 75.
[5]H. Niehus, J. Vac. Sci. Technol. A **5**, 751 (1987).
[6]David P. Smith, J. Appl. Phys. **38**, 340 (1967).
[7]J. A. Yarmoff and R. S. Williams, J. Vac. Sci. Technol. A **4**, 1274 (1986).
[8]A. G. J. de Wit, R. P. N. Bronckers, and J. M. Fluit, Surf. Sci. **82**, 177 (1979).
[9]M. Aono, C. Oshima, S. Zaima, S. Otani, and Y. Ishizawa, Jpn. J. Appl. Phys. **20**, 829 (1981).
[10]R. L. McEachern, D. L. Adler, D. M. Goodstein, G. A. Kimmel, B. R. Litt, D. R. Peale, and B. H. Cooper, Rev. Sci. Instrum. **59**, 2560 (1988).

[11]D. L. Adler and B. H. Cooper, Rev. Sci. Instrum. **59**, 137 (1988).
[12]The crystal was prepared by B. F. Addis of the Materials Science Center at Cornell University.
[13]Ming L. Yu and N. D. Lang, Phys. Rev. Lett. **50**, 127 (1983).
[14]G. A. Kimmel *et al.* (unpublished).
[15]D. M. Goodstein, S. A. Langer, and B. H. Cooper, J. Vac. Sci. Technol. A **6**, 703 (1988).
[16]A. D. Tenner, K. T. Gillen, and A. W. Kleyn, Nucl. Instrum. Methods Phys. Res. B **34**, 108 (1986).
[17]P. J. van den Hoek, A. D. Tenner, A. W. Kleyn, and E. J. Baerends, Phys. Rev. B **34**, 5030 (1986).
[18]M. J. Frisch *et al.*, GAUSSIAN 86, Carnegie-Mellon Quantum Chemistry Publishing Unit, 1984.
[19]D. M. Goodstein, Phys. Rev. B (to be published).
[20]M. Copel, T. Gustafsson, W. R. Graham, and S. M. Yalisove, Phys. Rev. B **33**, 8110 (1986).
[21]T. v. d. Hagen and E. Bauer, Phys. Rev. Lett. **47**, 579 (1981).
[22]T. M. Buck, G. H. Wheatley, and L. K. Verheij, Surf. Sci. **90**, 635 (1979), and references therein.
[23]For each trajectory, the impact parameter is defined as the point where the straight-line extrapolation of the initial incident trajectory intersects the plane containing the first-layer atoms. This definition must be considered when comparing coordinates along the beam direction ($\langle 1\bar{1}0 \rangle$ in Fig. 9, $\langle 001 \rangle$ in Fig. 10) from the impact-parameter plot with the coordinates of atoms in the first and second layers.
[24]G. Engelmann, W. Englert, S. Kato, and E. Taglauer, Nucl. Instrum. Methods Phys. Res. B **26**, 522 (1987).
[25]H. H. Brongersma, M. J. Sparnaay, and T. M. Buck, Surf. Sci. **71**, 657 (1978).